Whole-body and whole-organ 3D imaging of hypoxia using activatable covalent fluorescent probe compatible with tissue clearing

Daichi M. Sakamoto[1], Iori Tamura[1], Bo Yi[1], Sho Hasegawa[2], Yutaro Saito[1], Naoki Yamada[1†], Yoichi Takakusagi[3,4], Shimpei I. Kubota[5], Hiroshi Harada[6,7], Kenjiro Hanaoka[8], Masayasu Taki[9], Masaomi Nangaku[2], Kazuki Tainaka[10]*, and Shinsuke Sando[1,11]*

[1]Department of Chemistry and Biotechnology, Graduate School of Engineering, The University of Tokyo, 7-3-1 Hongo, Bunkyo-ku, Tokyo, 113-8656, Japan.

[2]Division of Nephrology and Endocrinology, Graduate School of Medicine, The University of Tokyo, 7-3-1 Hongo, Bunkyo-ku, Tokyo, 113-8654, Japan.

[3]Quantum Hyperpolarized MRI Team, Institute for Quantum Life Science, National Institutes for Quantum Science and Technology, 4-9-1 Anagawa, Inage, Chiba-city, 263-8555, Japan.

[4]Institute for Quantum Medical Science, National Institutes for Quantum Science and Technology, 4-9-1 Anagawa, Inage, Chiba-city, 263-8555, Japan.

[5]Division of Molecular Psychoimmunology, Institute for Genetic Medicine, Graduate School of Medicine, Hokkaido University, Kita-15, Nishi-7, Kita-ku, Sapporo, Hokkaido, 060-0815, Japan.

[6]Laboratory of Cancer Cell Biology, Graduate School of Biostudies, Kyoto University, Yoshida Konoe-cho, Sakyo-ku, Kyoto, 606-8501, Japan.

[7]Department of Genome Dynamics, Radiation Biology Center, Graduate School of Biostudies, Kyoto University, Yoshida Konoe-cho, Sakyo-ku, Kyoto, 606-8501.

[8]Division of Analytical Chemistry for Drug Discovery, Graduate School of Pharmaceutical Sciences, Keio University, 1-5-30 Shibakoen, Minato-ku, Tokyo, 105-8512, Japan.

[9]Institute of Transformative Bio-Molecules, Nagoya University, Furo, Chikusa, Nagoya, 464-8601, Japan.

[10]Department of System Pathology for Neurological Disorders, Brain Research Institute, Niigata University, 1-757 Asahimachidori, Chuo-ku, Niigata 951-8585, Japan.

[11]Department of Bioengineering, Graduate School of Engineering, The University of Tokyo, 7-3-1 Hongo, Bunkyo-ku, Tokyo, 113-8656, Japan.

[†]Present address: Department of Physiology, National Defense Medical College, Namiki, Tokorozawa, Saitama 359-8513, Japan.

ABSTRACT: Elucidation of biological phenomena requires imaging of microenvironments *in vivo*. Although the seamless visualization of *in vivo* hypoxia from the level of whole-body to single-cell has a great potential to discover unknown phenomena in biological and medical fields, no methodology for achieving it has been established thus far. Here, we for the first time report the whole-body and whole-organ imaging of hypoxia, an important microenvironment, at single-cell resolution using activatable covalent fluorescent probes compatible with tissue clearing. We initially focused on overcoming the incompatibility of fluorescent dyes and refractive index matching solutions (RIMSs), which has greatly hindered the development of fluorescent molecular probes in the field of tissue clearing. The fluorescent dyes compatible with RIMS were then incorporated into the development of activatable covalent fluorescent probes for hypoxia. We combined the probes with tissue clearing, achieving comprehensive single-cell-resolution imaging of hypoxia in a whole mouse body and whole organs.

It is known that not only the existence of specific biomolecules, but also their surrounding microenvironments, e.g. hypoxia, acidity, reactive oxygen species, and metal ions, play important roles in various physiological and pathological processes[1–5]. Artificial microenvironments are easily created *in vitro*, but have disparate influences on the cells than *in vivo* microenvironments[6–8]. Therefore, imaging and analyzing *in vivo* microenvironments is required to elucidate unknown biological phenomena.

Small molecule-based activatable fluorescent probes are a class of potent tools for observing transient targets such as *in vivo* microenvironments due to their high sensitivity and target adjustability by chemical modifications[9–12]. Various activatable fluorescent

probes for imaging *in vivo* microenvironments at single-cell resolution have been developed[13–16]. However, because of the poor penetration depth of light, fluorescent probes have a big hurdle to comprehensively visualize *in vivo* targets in the whole body or whole organ at single-cell resolution[17,18].

Tissue clearing, which renders biological tissues transparent by minimizing the differences in refractive index (RI) between tissue components, is a rapidly developing technique that enables depth-independent fluorescence imaging[19–24]. This technique allows 3D single-cell imaging and analysis of fluorescently labeled biomolecules without sectioning and other laborious processes. The combination of activatable fluorescent probes and tissue clearing has the potential to realize the seamless imaging of *in vivo* microenvironments from the level of whole-body to single-cell, which would enable unprecedented insight into previously under-characterized or overlooked biological processes.

Nevertheless, the application of activatable fluorescent probes in the field of tissue clearing has two major obstacles. Firstly, there are incompatibilities between regular fluorescent dyes and refractive index matching solutions (RIMSs) in which fluorescently labeled tissue is immersed during observation. The brightness of several fluorescent dyes was reported to be decreased in certain RIMSs[25–27]. Secondly, unfixable fluorescent small molecules will be washed out in the process of tissue clearing because the integrity of cell membranes is compromised by detergents and organic solvents for rendering tissue transparent[28,29]. Thus, activatable "covalent" fluorescent probes, which are fixed at the reaction site, are desirable to be used in tissue clearing. Although a detergent-free, pH-adjustable tissue clearing method was reported for preserving cell membranes and for keeping unfixable ionic probes in the cell, it greatly limits the variety of activatable fluorescent probes and is inherently unable to achieve a high level of tissue transparency[30].

On the other hand, great efforts have been devoted to developing covalent fluorescent probes targeting various microenvironments such as hypoxia[31,32], reactive oxygen species (ROS)[33], and metal ions[34]. However, these probes cannot be readily used in conjunction with tissue clearing due to issues arising from their incompatibility with RIMSs. Thus, it is crucial to develop an activatable covalent fluorescent probe for a microenvironment that shows optimal photophysical properties in RIMSs, and to demonstrate its application in tissue clearing imaging.

In this research, we demonstrate a methodology for seamlessly imaging *in vivo* microenvironments from the level of whole-body to single-cell. We focus on imaging one of the most important microenvironments, hypoxia. Specifically, hypoxia in a mouse is covalently labeled with an activatable fluorescent probe while the organism is alive, followed by tissue clearing of the whole body and comprehensive 3D imaging of hypoxia at single-cell resolution (Figure 1a). In order to achieve this, we first investigate the compatibility of major fluorescent dyes and RIMSs, and deduce solutions to overcome the incompatibility by focusing on the chemical mechanisms for their fluorogenicity (Figure 1b-left). Then, using these fluorescent dyes, we develop activatable covalent fluorescent probes targeting *in vivo* hypoxia (Figure 1b-right). Finally, we demonstrate 3D imaging of hypoxia in the cleared whole body and whole organ.

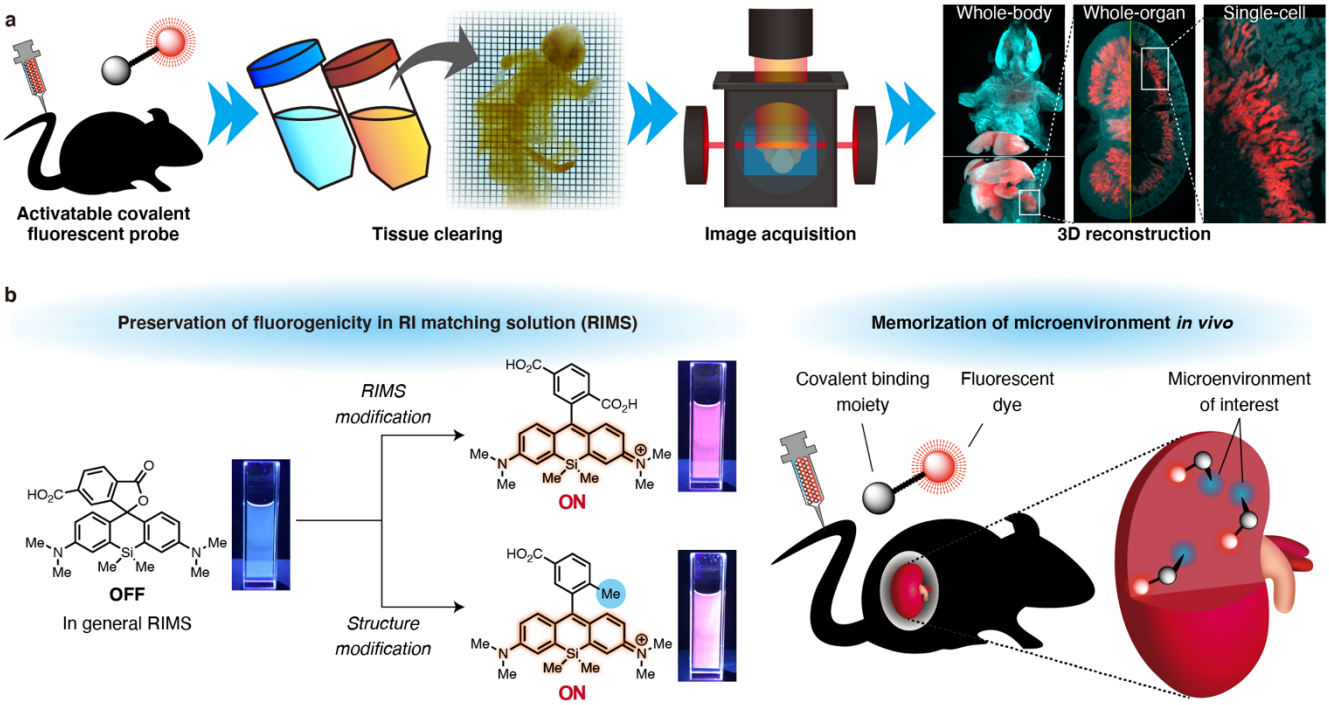

Fig. 1 Overview of this study. a Schematic workflow for 3D imaging of microenvironments using activatable fluorescent covalent probes compatible with tissue clearing. **b** Two requisites for activatable covalent fluorescent probe for microenvironment imaging with tissue clearing.

RESULTS

Investigation of the compatibility of representative fluorescent dyes with RIMSs. We began by examining fluorescent dyes that are usable with tissue clearing. Xanthene dyes and cyanine dyes, especially the Alexa Fluor series, have been frequently used in most tissue clearing methods. Recently, however, several fluorescent dyes including Alexa Fluor dyes have been reported to change their emission wavelengths and brightness in RIMSs[25]. In this research, we focused on fluorescein isothiocyanate (FITC), tetramethylrhodamine (TAMRA), and Si-Rhodamine as representative xanthene-type dyes, and cyanine 3 and 5 (Cy3 and Cy5) as representative cyanine dyes to be investigated (Figure 2a, upper line). We then measured the photophysical properties of those fluorescent dyes in representative organic solvent- and aqueous-based RIMSs, BABB (mixture of benzyl alcohol and benzyl benzoate at 1:2 (v/v))[35] and CUBIC-R (45% (w/w) antipyrine, 30% (w/w) nicotinamide)[36] (Figures 2b and 2c). The results are shown in Figure 2d. The fluorescence brightness of TAMRA, Cy3, and Cy5 in both RIMSs was higher than that in PBS. On the other hand, the fluorescence of FITC and Si-Rhodamine was too weak to be determined in BABB, and their brightness in CUBIC-R was attenuated by less than 3% of that in PBS.

Further investigation and optimization for the compatibility of fluorescent dyes with RIMSs. These changes in the photophysical properties of dyes in RIMSs are plausible because RIMSs provide different environments to fluorescent dyes than in water. However, no research has focused on their quenching mechanisms and how to preserve their fluorogenicity. We then considered quenching mechanisms of FITC and Si-Rhodamine in RIMSs and deduced methods to preserve their fluorescence. We first gave attention to the considerable attenuation of molar extinction coefficients and the different absorption spectra of FITC and Si-Rhodamine in BABB and CUBIC-R, as evidence that structural changes in these dyes were induced in RIMSs (Figure 2d, Supplementary Figures 1–3). It is known that xanthene dyes containing an intramolecular spiro ring show fluorogenicity upon ring opening, based on the π conjugation of the xanthene structure, but never show fluorogenicity with the spiro ring in the closed form. In addition, FITC tends to exist in the fluorescent open form under basic conditions[37], while Rhodamine tends to exist in the fluorescent open form under acidic conditions[38] (Figures 2f and 2g). From these understandings, FITC and Si-Rhodamine were assumed to show improved fluorogenicity in RIMS with adjusted acidity. Therefore, we developed acidified BABB (BABB with 10 mM trifluoroacetic acid), basified BABB (BABB with 1 mM 1,1,3,3-tetramethylguanidine), and acidified CUBIC-R (CUBIC-R with 2% (w/w) HCl) through investigations of optimized conditions (Figure 2b and 2c, see Supplementary Figures 7–9 for the optimization of conditions). Rather than developing an original basified CUBIC-R solution, we used CUBIC-R+ (CUBIC-R with 0.5% (v/v) *N*-butyldiethanolamine (NBDEA)) which was reported by K. Matsumoto *et al*.[39]. FITC showed higher brightness both in basified BABB and CUBIC-R+ than in PBS (Figures 2d and 2f), while Si-Rhodamine showed similar brightness both in acidified BABB and in acidified CUBIC-R as in PBS (Figures 2d and 2g).

Apart from the RIMS modification, xanthene-type dyes that cannot form a spiro ring in their structure were assumed to show stable photophysical properties independent of components of RIMSs. On this account, we gave attention to TokyoGreen[40,41], Me-Si-Rhodol[42], Me-Si-Rhodamine[43–45], PO-Rhodamine[46] as representative non-spiro xanthene-type dyes (Figure 2a, lower line) and measured their photophysical properties in RIMSs (Figure 2e). All non-spiro xanthene-type dyes except TokyoGreen showed higher brightness in regular RIMSs than in PBS. The brightness of TokyoGreen in regular RIMSs was surprisingly much lower than in PBS. Based on the different shapes of absorption spectra of TokyoGreen in RIMSs from that in PBS (Supplementary Figures 1–3), we expected this was due to the protonation of the hydroxy group of the xanthene chromophore. We then measured the photophysical properties of TokyoGreen in basified RIMSs and observed an increase in brightness (Figure 2e). As described above, we suggested two methods to address the incompatibility of xanthene-type fluorescent dyes with RIMS, acidity modification of RIMS, and the use of non-spiro xanthene-type dyes.

Furthermore, we attempted to expand the variety of fluorescent dyes compatible with tissue clearing and gave attention to boron-dipyrromethene (BODIPY) because no dipyrromethene dyes have been applied in tissue clearing. BODIPY is known for its photophysical stability in various organic solvents and was accordingly expected to show high brightness in RIMSs that induce different environments than in water[47]. We measured its photophysical properties and found BODIPY showed higher brightness in BABB than in PBS, although its brightness in CUBIC-R was attenuated to about 17% of that in PBS (Figure 2e). This indicates the compatibility of BODIPY with organic solvent-based tissue clearing.

From the investigations described above, we identified ten fluorescent dyes with various absorbance (450–750 nm) and fluorescence (500–800 nm) wavelengths usable for tissue clearing imaging (Figures 2h, 2i, and Supplementary Figure 10). This knowledge will be essential for developing activatable fluorescent probes for application with tissue clearing.

Design of activatable covalent fluorescent probes for detecting hypoxia. Next, we aimed to develop activatable fluorescent probes for an *in vivo* microenvironment using ten fluorescent dyes compatible with RIMSs. In this research, hypoxia, which is one of the most important microenvironments, was selected as an imaging target. Hypoxia refers to a biological condition with relatively low oxygen concentration caused by the imbalance of oxygen supply and consumption, and is recognized to be an index of not only tissue activity but also physiological disorders[48–52].

We applied pimonidazole, a widely used component of established hypoxia probes (Figure 3a left). 2-Nitroimidazole compounds such as pimonidazole are reduced to 2-aminoimidazole compounds by intracellular reductases selectively under hypoxic conditions, forming a covalent bond with an intracellular nucleophile such as a protein or nucleic acid[53] (Figure 3b). This ability to form a covalent bond with an intracellular biomolecule is expected to allow probes to be retained during the harsh tissue clearing process[28,29]. We designed and synthesized 10 Pimo-Dyes that are chemical conjugates between pimonidazole and each fluorescent dye compatible

with RIMSs (Figure 3a right). Each Pimo-Dye was synthesized by the coupling reaction between the terminal amino group of Pimo-NH_2 and the isothiocyanate group or the carboxyl group of each fluorescent dye shown in Figure 2a. The synthesized compounds were identified by NMR and MS analyses (see Materials and Methods for the Synthetic procedures in detail). These Pimo-Dyes are expected to be fixed in hypoxic cells while the organism is alive, and after tissue clearing, provide the spatial information of *in vivo* hypoxia.

Evaluation of the ability of activatable fluorescent probes for hypoxia detection in cells. To evaluate the efficacy of the synthesized Pimo-dyes in detecting hypoxia, we first checked whether each Pimo-Dye selectively stained cultured cells under hypoxic conditions (see Materials and Methods for the procedure of Hypoxic cell imaging in detail). By fluorescence imaging of C26 cells incubated with each Pimo-Dye under hypoxic (1% O_2) or normoxic (*ca.* 20% O_2) conditions, we showed that Pimo-Si-Rhodamine, Pimo-Me-Si-Rhodol, and Pimo-BODIPY stained hypoxic cells selectively (Figure 3c). It was also confirmed that all dyes with no pimonidazole conjugation did not stain either hypoxic and normoxic cells (Supplementary Figure 11). According to quantitative analysis with flow cytometry, median fluorescence intensities of hypoxic cells derived from Pimo-Si-Rhodamine, Pimo-Me-Si-Rhodol, and Pimo-BODIPY were respectively 58, 12, and 14 times higher than that of normoxic cells (Figures 3d–f). These results indicate that these three Pimo-Dyes have the ability of hypoxia-dependent cell labeling.

We then investigated why the other seven Pimo-Dyes did not stain hypoxic cells by imaging live cells during incubation with each Pimo-Dye in order to observe their membrane permeability (see Materials and Methods for the procedure of Live cell imaging in detail). We observed that only Pimo-Si-Rhodamine, Pimo-Me-Si-Rhodol, and Pimo-BODIPY passed through cell membranes and stained cytoplasms (Figure 3g). In contrast, the fluorescence of the other seven Pimo-Dyes was not detectable in cells, or existed only as granular particles in cells (Figure 3g, Supplementary Figure 12). Considering this result, the seven Pimo-Dyes that did not stain hypoxic cells were deduced to either be membrane impermeable or captured in endosomes in which the environment was not appropriate for the reaction of Pimo-Dye.

Evaluation of the ability of activatable fluorescent probes for hypoxia detection *in vivo*. We then evaluated the capability of Pimo-Si-Rhodaimne, Pimo-Me-Si-Rhodol, and Pimo-BODIPY which could stain hypoxic cells, to detect hypoxia *in vivo*. We focused on detecting renal hypoxia in mice using these Pimo-Dyes, as healthy rodents are known to have severe hypoxia (10 mmHg or less pO_2) in their renal outer medulla[54,55]. The kidney sample of a mouse was collected after intravenous injection of the mixture of pimonidazole and each Pimo-Dye followed by immunohistochemical (IHC) staining of pimonidazole on the kidney slice (Supplementary Figure 13a, see Materials and Methods for the procedures of Animal experiments and IHC staining of pimonidazole in detail). By fluorescence imaging of these kidney slices, fluorescence signal from each Pimo-Dye was observed in the outer medulla, in the same region indicated by pimonidazole staining (Supplementary Figures 13b–d). We then attempted to confirm the distribution of the Pimo-Dye in the kidney to rule out the possibility that the Pimo-Dye reached only the outer medulla. A kidney was extracted from a mouse injected with Pimo-Me-Si-Rhodol and immediately immersed into O.C.T. compound and frozen. Then, the frozen kidney was sectioned, and the fluorescence of the section was observed without any further treatment. All regions in the kidney section including the renal cortex, inner medulla, and renal pelvis were stained with Pimo-Me-Si-Rhodol, indicating the Pimo-Dyes was distributed all over the kidney (Supplementary Figure 14). Furthermore, no fluorescence was observed in the kidneys of mice injected with each dye with no pimonidazole conjugation (Supplementary Figure 15). Based on these results, the three Pimo-Dyes were validated to detect *in vivo* hypoxia at the same quality as pimonidazole for probing severe hypoxia (10 mmHg or less pO_2).

3D imaging of hypoxia in the whole organ and whole body using activatable fluorescent probes. Using Pimo-Dyes applicable to *in vivo* hypoxia detection, we conducted 3D hypoxia imaging of the whole kidney with tissue clearing (Figure 4a). We first established a simple tissue clearing protocol involving 18 hours of delipidation with 10% (v/v) 1,2-hexanediol (HxD), 0.02% (v/v) NBDEA aqueous solution[56] followed by RI matching (Figure 4b). For the use of BABB-based RIMSs, dehydration steps were added after delipidation. All BABB-based RIMSs were able to render kidneys highly transparent regardless of the additives (Supplementary Figure 16). On the other hand, CUBIC-R-based RIMSs had a lower ability to render kidneys transparent compared with BABB-based RIMSs (Supplementary Figure 16), suggesting that BABB-based RIMSs are more appropriate for whole-body clearing of mice with bones and adipose tissues.

Kidneys labeled with each Pimo-Dye (Pimo-Si-Rhodamine, Pimo-Me-Si-Rhodol, and Pimo-BODIPY) were cleared through tissue clearing with BABB-based RIMSs, then observed with a light-sheet fluorescent microscope (LSFM). We succeeded in visualizing renal hypoxia three-dimensionally using each Pimo-Dye (Figures 4c, 4d, Supplementary Figure 17a, and Supplementary Movies 1, 2). In addition, similar results were obtained through tissue clearing with CUBIC-R-based RIMSs (Supplementary Figures 17b–d). In summary, 3D imaging of renal hypoxia was validated using Pimo-Me-Si-Rhodol and Pimo-BODIPY with regular BABB and CUBIC-R, and using Pimo-Si-Rhodamine with originally developed acidified BABB and acidified CUBIC-R.

Furthermore, we conducted the simultaneous staining of hypoxia and blood vessels in the kidney. It has been reported that major renal blood vessels and partial glomerular capillaries can be labeled with Evans blue[57,58]. We prepared a kidney sample in which blood vessels were labeled with Evans blue, and in which hypoxic regions were labeled with Pimo-BODIPY. By fluorescence imaging with LSFM, we succeeded in the simultaneous 3D visualization of renal hypoxia (green in Figure 4e) and blood vessels (red in Figure 4e) (Supplementary Movie 2).

Finally, we demonstrated whole-body 3D imaging of hypoxia. A mouse injected with Pimo-Me-Si-Rhodol was sacrificed with perfusion fixation, followed by the removal of the skin and bowel contents (Figure 4f). The mouse sample was then cleared by

delipidation with 10% (v/v) HxD and 0.02% (v/v) NBDEA, decalcification with an aqueous solution of 15% (w/v) imidazole and 10% (w/v) ethylenediaminetetraacetic acid (EDTA)[36], a second step of delipidation, and RI matching with BABB after gradual dehydration with MeOH (Figure 4g, see Materials and Methods for the Animal experiment procedure and the Tissue clearing protocol in detail). The tissue clearing protocol optimized in this research enabled a high level of transparency of the adult mouse whole body (Figure 4h). We succeeded in visualizing the presence of hypoxia deep inside throughout the cleared mouse whole body with LSFM (Figures 4i and 4l). Strong fluorescence was observed not only in the kidneys but also in the liver. The magnified views showed that the outer medulla was stained in the kidney (Figure 4k), and the vicinity of the central veins was stained in the liver (Figure 4j). Additionally, relatively weak fluorescence derived from Pimo-Me-Si-Rhodol was observed in the spleen, the dorsal muscles, and around the eyes (Figures 4h and 4l). Furthermore, no fluorescence was observed from the cleared mouse whole body when injected with Me-Si-Rhodol, indicating that the signals of Pimo-Me-Si-Rhodol were based on the reactivity of 2-nitroimidazole moiety under hypoxic conditions (Figure 4m). With these results, seamless hypoxia imaging from the level of whole-body to single-cell was demonstrated by the combination of an activatable covalent fluorescent probe and tissue clearing.

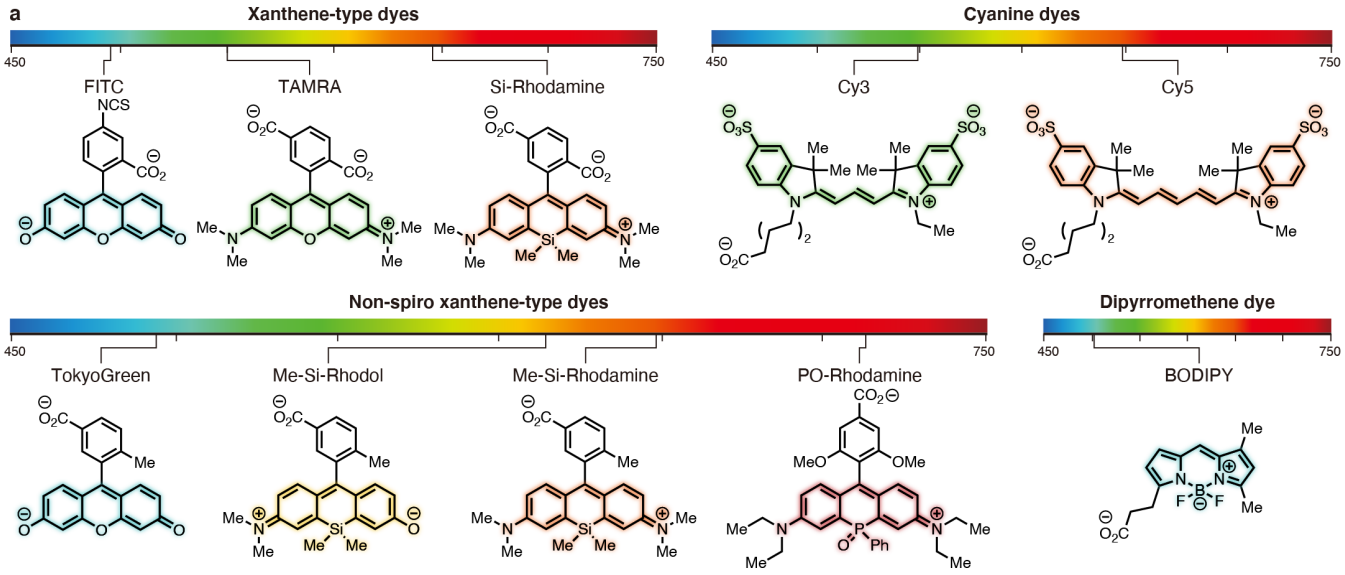

b Organic solvent-based RIMS

BABB	1:2 (v/v) benzyl alcohol, benzyl benzoate
Acidified BABB	BABB with 10 mM trifluoroacetic acid
Basified BABB	BABB with 1 mM 1,1,3,3-tetramethylguanidine

c Aqueous-based RIMS

CUBIC-R	45% (w/w) antipyrine, 30% (w/w) nicotinamide, 25% (w/w) water
Acidified CUBIC-R	45% (w/w) antipyrine, 30% (w/w) nicotinamide, 22% (w/w) water, 3% (w/w) HCl
CUBIC-R+	CUBIC-R with 0.5% (v/v) *N*-butyldiethanolamine

d

Dye	Solvent	λ_{abs}(nm)	λ_{em}(nm)	ε($M^{-1}cm^{-1}$)	ϕ_{fl}	Brightness (ε×ϕ_{fl})
FITC	PBS	495	519	86,500	0.55	47,600
	BABB	464	536	400	n.d.	n.d.
	Basified BABB	508	530	115,000	0.60	69,000
	CUBIC-R	461	530	8,800	0.14	1,200
	CUBIC-R+	507	530	104,400	0.53	55,300
TAMRA	PBS	550	579	81,600	0.43	35,100
	BABB	552	581	40,300	0.91	36,700
	CUBIC-R	556	582	77,800	0.63	49,000
Si-Rhodamine	PBS	645	668	96,600	0.37	35,800
	BABB	n.d.	678	n.d.	n.d.	n.d.
	Acidified BABB	663	682	49,000	0.71	34,800
	CUBIC-R	655	673	1,600	0.61	1,000
	Acidified CUBIC-R	663	682	64,600	0.48	31,000
Cy3	PBS	549	565	162,400	0.06	9,700
	BABB	564	582	122,600	0.39	47,800
	CUBIC-R	561	577	140,300	0.53	74,400
Cy5	PBS	647	688	315,600	0.22	69,400
	BABB	666	690	246,400	0.53	130,600
	CUBIC-R	660	683	284,900	0.61	173,800

e

Dye	Solvent	λ_{abs}(nm)	λ_{em}(nm)	ε($M^{-1}cm^{-1}$)	ϕ_{fl}	Brightness (ε×ϕ_{fl})
Tokyo Green	PBS	493	512	62,600	0.84	52,600
	BABB	464	526	18,500	0.40	7,400
	Basified BABB	513	530	74,600	0.87	64,900
	CUBIC-R	464	530	17,700	0.10	1,800
	CUBIC-R+	513	529	62,600	0.78	48,900
Me-Si-Rhodol	PBS	614	633	105,800	0.28	29,600
	BABB	578	639	40,000	0.85	34,000
	CUBIC-R	612	645	60,800	0.68	41,300
Me-Si-Rhodamine	PBS	648	665	79,400	0.37	29,400
	BABB	664	681	89,600	0.72	64,500
	CUBIC-R	662	679	86,400	0.52	44,900
PO-Rhodamine	PBS	713	739	130,300	0.12	15,600
	BABB	716	736	157,300	0.48	75,500
	CUBIC-R	720	743	145,000	0.14	20,300
BODIPY	PBS	503	512	97,100	0.94	91,200
	BABB	511	520	113,600	0.89	101,100
	CUBIC-R	510	521	96,400	0.16	15,400

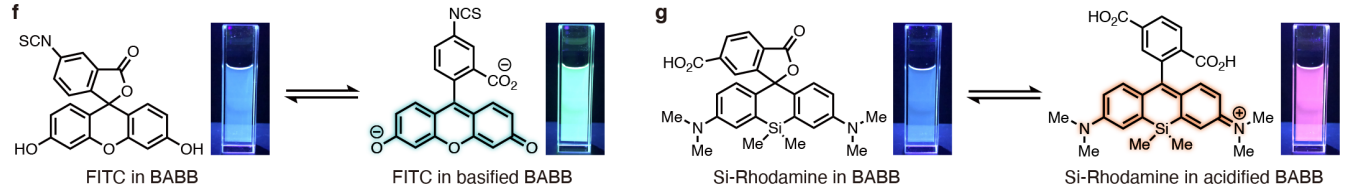

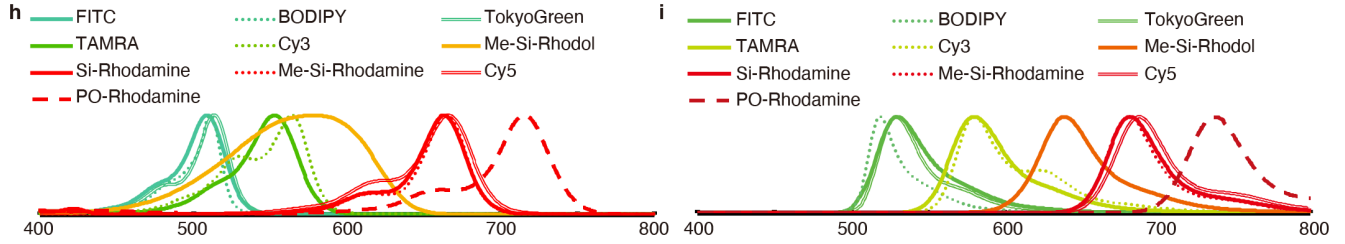

Fig. 2 Photophysical properties of fluorescent dyes in RIMS. a Fluorescent dyes evaluated in this study. Their maximum absorption wavelengths in PBS are shown in the color bars. **b**,**c** Components of organic solvent-based RIMS (**b**) and aqueous-based RIMS (**c**) used in this study. **d**,**e** Photophysical properties of fluorescent dyes (1 μM) in PBS and each RIMS at 25 °C. n.d.: not determined. **f**,**g** Plausible mechanism of fluorescence on/off switching for FITC (**f**) and Si-Rhodamine (**g**) in RIMS. Photographs are the solution of 1 μM FITC in BABB (left of **f**) or in basified BABB (right of **f**), and the solution of 10 μM Si-Rhodamine in BABB (left of **g**) or in acidified BABB (right of **g**) under irradiation of UV light at 365 nm. **h**,**i** Normalized absorption (**h**) and fluorescence (**i**) spectra of fluorescent dyes (1–6 μM) in BABB (or basified BABB for FITC and TokyoGreen and acidified BABB for Si-Rhodamine) at 25 °C. The excitation wavelength used for each dye is indicated under λ_{abs} in the charts (**d**,**e**).

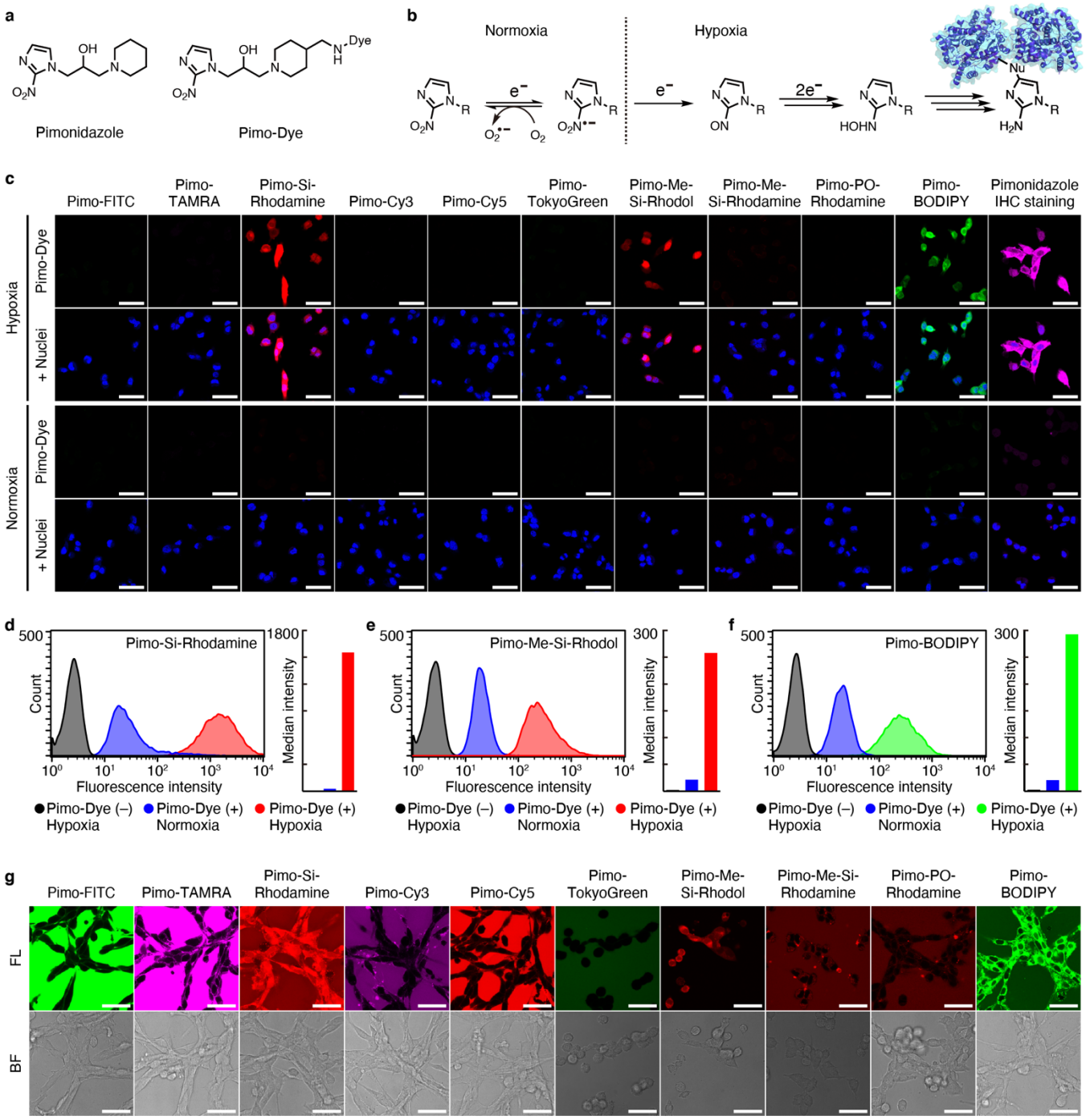

Fig. 3 The ability of designed activatable fluorescent probes for hypoxia detection. a Chemical structures of pimonidazole and the designed fluorescent probe for hypoxia, Pimo-Dye. **b** Proposed mechanism for the binding of nitroimidazole compounds to cellular nucleophiles under hypoxic conditions. **c** CLSM images of C26 cells incubated with 10 μM of each Pimo-Dye or pimonidazole under hypoxic (1% O_2) or normoxic (*ca.* 20% O_2) conditions for 2 h at 37 °C. Nuclei of cells were stained with Hoechst 33342. Scale bar: 50 μm. **d**,**e**,**f** Quantitative analysis of hypoxia-dependent fluorescence staining of C26 cells, incubated with 10 μM of Pimo-Si-Rhodamine (**d**), Pimo-Me-Si-Rhodamine (**e**), and Pimo-BODIPY (**f**) under the same condition as **c**, measured with flow cytometry. **g** CLSM images of live C26 cells incubated with 10 μM of each Pimo-Dye for 60 minutes under normoxic conditions at 37 °C. Scale bar: 50 μm. FL: fluorescence, BF: bright field.

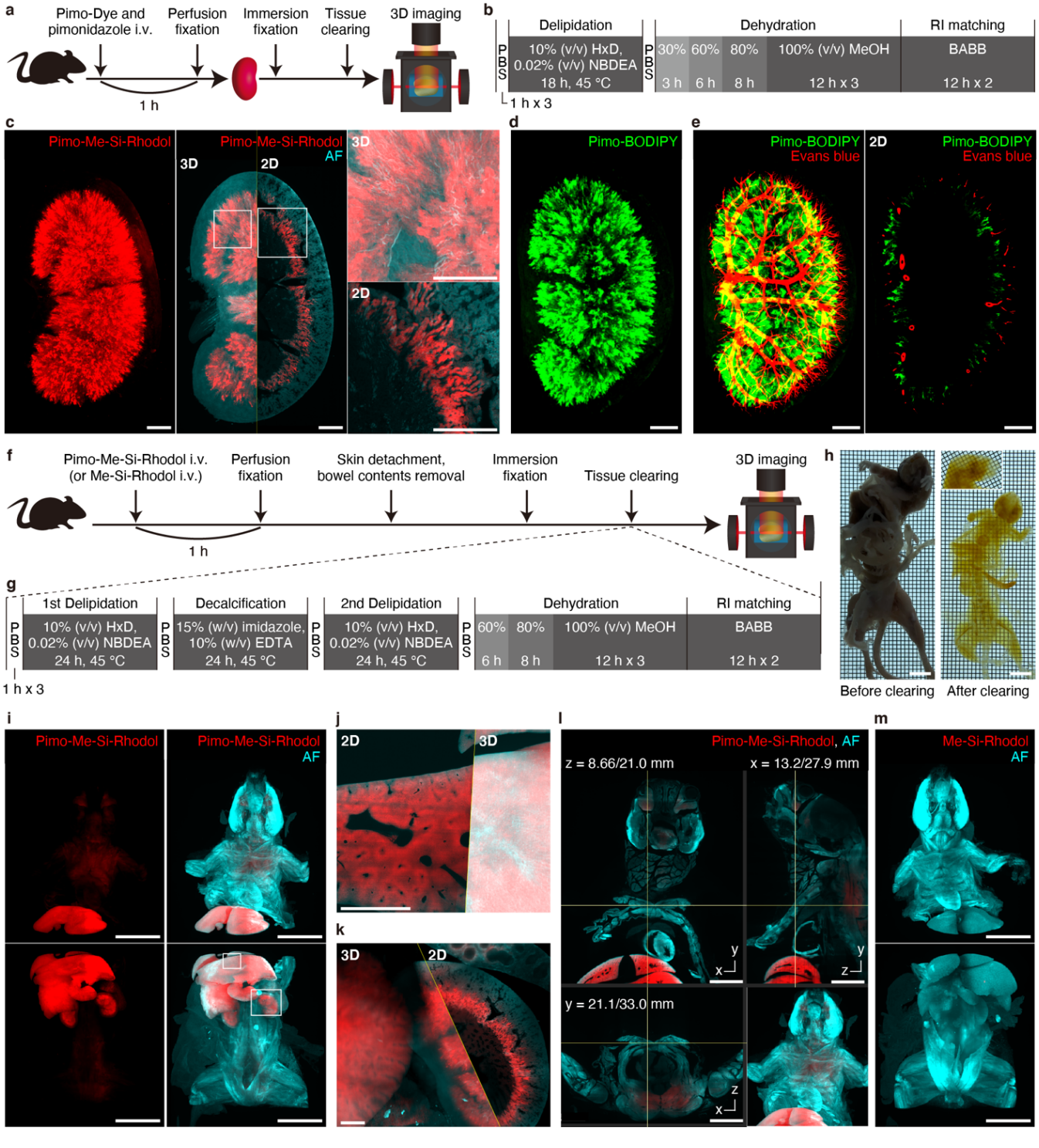
a
Pimo-Dye and pimonidazole i.v.
Perfusion fixation
Immersion fixation
Tissue clearing
3D imaging
1 h
b
Delipidation
Dehydration
RI matching
PBS
10% (v/v) HxD, 0.02% (v/v) NBDEA
18 h, 45 °C
30%
60%
80%
100% (v/v) MeOH
BABB
3 h
6 h
8 h
12 h x 3
12 h x 2
1 h x 3
c
Pimo-Me-Si-Rhodol
3D
2D
AF
d
Pimo-BODIPY
e
Pimo-BODIPY
Evans blue
f
Pimo-Me-Si-Rhodol i.v.
(or Me-Si-Rhodol i.v.)
Perfusion fixation
Skin detachment, bowel contents removal
Immersion fixation
Tissue clearing
3D imaging
1 h
g
1st Delipidation
Decalcification
2nd Delipidation
Dehydration
RI matching
10% (v/v) HxD, 0.02% (v/v) NBDEA
24 h, 45 °C
15% (w/v) imidazole, 10% (w/v) EDTA
24 h, 45 °C
60%
80%
100% (v/v) MeOH
BABB
6 h
8 h
12 h x 3
12 h x 2
1 h x 3
h
Before clearing
After clearing
i
Pimo-Me-Si-Rhodol
AF
j
2D
3D
k
3D
2D
l
Pimo-Me-Si-Rhodol, AF
z = 8.66/21.0 mm
x = 13.2/27.9 mm
y = 21.1/33.0 mm
m
Me-Si-Rhodol
AF

Fig. 4 Whole-organ and whole-body imaging of hypoxia. a Workflow for the whole-organ 3D imaging with tissue clearing. **b** Tissue clearing protocol for mouse organs used in this study. **c** 3D and 2D visualization of renal hypoxia labeled with Pimo-Me-Si-Rhodol (red) and autofluorescence (AF) by 488 nm excitation (cyan). Pixel resolution: 4.1 μm, scale bar: 1 mm. **d** 3D visualization of renal hypoxia labeled with Pimo-BODIPY (green). Pixel resolution: 4.1 μm, scale bar: 1 mm. **e** 3D and 2D visualization of renal hypoxia labeled with Pimo-BODIPY (green) and blood vessels labeled with Evans blue (red). Pixel resolution: 4.1 μm, scale bar: 1 mm. **f** Workflow for the whole-body 3D imaging with tissue clearing. **g** Tissue clearing protocol for the mouse whole body used in this study. **h** Pictures of the whole body before and after tissue clearing. Scale bar: 10 mm. **i** Whole-body imaging of hypoxia labeled with Pimo-Me-Si-Rhodol (red) and autofluorescence (AF) by 488 nm excitation (cyan). Pixel resolution: 12.9 μm, scale bar: 10 mm. **j**,**k** 3D and 2D visualization of liver ROI (**j**) and kidney ROI (**k**), shown in **i**, observed with a high power objective lens. Pixel resolution: 4.1 μm, scale bar: 1 mm. **l** 2D slices of the coronal view (upper left), sagittal view (upper right), transverse view (lower left) and the whole image of the upper body (lower right). Pixel resolution: 12.9 μm, scale bar: 5 mm. **m** Whole-body imaging of the mouse injected with Me-Si-Rhodol as a negative control. Pixel resolution: 12.9 μm, scale bar: 10 mm.

DISCUSSION

We demonstrated the seamless imaging of hypoxia from the level of whole-body to single-cell using activatable covalent fluorescent probes, enabled by solving the incompatibility between fluorescent dyes and RIMS for tissue clearing. To the best of our knowledge, this is the first example of single-cell-level whole-body imaging of hypoxia with tissue clearing.

The investigation of the photophysical properties of representative fluorescent dyes used for bioimaging demonstrated that the fluorescence of FITC and Si-Rhodamine was dramatically decreased in RIMSs (BABB and CUBIC-R) (Figure 2d). We then developed appropriate RIMSs for FITC and Si-Rhodamine by modifying the acidity of RIMSs (acidified BABB, basified BABB, acidified CUBIC-R). In addition, we focused on modifying the structure of xanthene-type dyes to overcome their incompatibilities with regular RIMSs and demonstrated the usability of non-spiro xanthene-type dyes (Figures 2a and 2e). Understanding these photophysical properties of fluorescent dyes in RIMS will contribute to improving the imaging quality and facilitating more accurate and reliable measurements of a target of interest. Eventually, we determined that ten fluorescent dyes with various absorption (450–750 nm) and fluorescence (500–800 nm) wavelengths are usable for tissue clearing imaging (Figures 2h, 2i, and Supplementary Figure 10). This information will be the foundation for the development of new fluorescent probes for application with tissue clearing.

Three covalent hypoxia probes developed using tissue clearing-compatible fluorescent dyes (Pimo-Si-Rhodamine, Pimo-Me-Si-Rhodol, and Pimo-BODIPY) labeled cells only when cultured under hypoxic conditions (Figures 3c–f), as well as hypoxic tissue *in vivo* (Supplementary Figure 13). Incidentally, these Pimo-Dyes could also be attractive alternatives to pimonidazole IHC for *in vivo* hypoxia detection irrespective of whether tissue clearing is used or not, due to their higher signal-to-background ratio, attributed to them circumventing the need for antibody staining (Supplementary Figures 13b–d). The reason why the other Pimo-Dyes did not work was presumably because of their low cell membrane permeability (Figure 3g, Supplementary Figure 12). The results regarding cell membrane permeability of all Pimo-Dyes could provide beneficial information for designing fluorescent molecular probes for detecting additional targets *in vivo*.

The combination of Pimo-Dyes and tissue clearing realized the seamless imaging of hypoxia from the level of whole-body to single-cell (Figure 4). Pimo-Me-Si-Rhodol and Pimo-BODIPY enabled 3D hypoxia imaging with regular BABB (Figures 4c, 4d, and Supplementary Movies 1, 2) and CUBIC-R (Supplementary Figures 17c and 17d). Since Si-Rhodamine was not capable of fluorescing in regular RIMSs, we developed novel RIMSs consisting of acidified BABB and acidified CUBIC-R, and eventually achieved 3D hypoxia imaging using Pimo-Si-Rhodamine (Supplementary Figures 17a and 17b). In addition, we observed the 3D landscape of renal hypoxia and blood vessels using Pimo-BODIPY and Evans blue (Figure 4e). As clearly demonstrated in Figure 4e (left *vs* right) and Supplementary Movie 2, the 3D visualization provided a much clearer interpretation of the hypoxia-vascular relationship than the 2D visualization.

In whole-body hypoxia imaging, the strong signal derived from Pimo-Me-Si-Rhodol was detected not only in the kidney (Figure 4k) but also in the liver (Figure 4j). The oxygen pressure in the renal outer medulla has been reported to be about 10 mmHg under a regular physiological condition by the direct measurement of pO_2 with a polarographic micro-needle electrode[59]. Our results of renal hypoxia imaging were consistent with these previous reports. As for the liver, it is already known that the vicinity of the central veins (CVs) is relatively hypoxic, but not to an extent which is detectable with pimonidazole[60,61]. However, our results indicated that the wide region around the CV in the liver was severely hypoxic (Figure 4j). The region labeled by Pimo-Me-Si-Rhodol in the liver was highly merged with the region where carbonic anhydrase IX (CA IX), an endogenous hypoxia-related marker, was expressed (Supplementary Figure 18). This colocalization verifies that Pimo-Me-Si-Rhodol detected *in vivo* severe hypoxia while the organism was alive. Considering that the liver is the organ responsible for the metabolism and excretion of lipophilic xenobiotics[60], a process requiring significant oxygen consumption, it is possible that the fluorescence observed around the CV indicates that severe hypoxia transiently emerged as a result of the metabolism of Pimo-Me-Si-Rhodol. On the other hand, weak fluorescence of Pimo-Me-Si-Rhodol was detected in the spleen, in which hypoxia has been previously reported to exist[62]. Weak fluorescence was also observed in tissues where hypoxia has not been previously indicated, such as around the eyes and in the dorsal muscles (Figures 4i and 4l). Further investigation is needed to elucidate the physiological significance of these hypoxic regions observed in this study.

As shown in the above results, the combination of tissue clearing and compatible activatable covalent fluorescent probes enables seamless microenvironment imaging from the level of whole-body to single-cell. While we targeted hypoxia with pimonidazole-based activatable fluorescent probes, various other microenvironments and molecular activities can be studied by utilizing alternative reactive moieties developed in the field of chemical biology[33,34,63].

Furthermore, fluorescent molecular probes have another great advantage. They can be synthesized in large amounts at a reasonable cost. This enhances the feasibility of the simultaneous whole-body analysis of multiple samples, which is troublesome to implement with antibodies and transgenic animals. The comparative analysis of multiple imaging data of microenvironments acquired under various conditions is conceivable to elucidate unknown microenvironment-related associations between different organs or tissues. In the future, the methodology realized in this study is expected to make a significant contribution to the exploration of previously unknown biological phenomena and their role in pathological processes.

ASSOCIATED CONTENT

Supplementary Information
Supplementary Movie 1
Supplementary Movie 2

AUTHOR INFORMATION

Corresponding Author

*Kazuki Tainaka: kztainaka@bri.niigata-u.ac.jp
*Shinsuke Sando: ssando@chembio.t.u-tokyo.ac.jp

Author Contributions

K.T. and S.S. conceived the project and provided resources and supervision. D.M.S., Y.S., K.T., and S.S. designed experiments. D.M.S., I.T., B.Y., Y.S., K.H., and M.T. performed the preparation of chemical probes. D.M.S., I.T., B.Y., S.H., N.Y., Y.T., S.I.K, H.H, M.N., and K.T. performed biological experiments and analyses. D.M.S., Y.S., and S.S. wrote the manuscript, which was edited by all co-authors.

ACKNOWLEDGMENT

We thank Dr. Hiroshi Nonaka (Kyoto University) for the fruitful discussion and advice. We thank Dr. Masafumi Kuroda (The University of Tokyo) for the use of the Light-Sheet Fluorescence Microscope. We thank Esther Darley for the careful proofreading and comments on this manuscript. This research was supported by JSPS KAKENHI [grant number JP19H00919 (to S.S.)], MEXT Q-LEAP [grant number JPMXS0120330644 to S.S.], The Precise Measurement Technology Promotion Foundation (to Y.S.), and AMED [grant number JP223fa727001s0801 (to Y.S.)].

REFERENCES

1. Tu, Z. *et al.* Design of therapeutic biomaterials to control inflammation. *Nat. Rev. Mater.* **7**, 557–574 (2022).
2. Singleton, D. C., Macann, A. & Wilson, W. R. Therapeutic targeting of the hypoxic tumour microenvironment. *Nat. Rev. Clin. Oncol.* **18**, 751–772 (2021).
3. Wang, S. *et al.* Fluorescence imaging of pathophysiological microenvironments. *Chem. Soc. Rev.* **50**, 8887–8902 (2021).
4. Schwartz, L., Peres, S., Jolicoeur, M. & da Veiga Moreira, J. Cancer and Alzheimer's disease: intracellular pH scales the metabolic disorders. *Biogerontology* **21**, 683–694 (2020).
5. Iovan, D. A., Jia, S. & Chang, C. J. Inorganic chemistry approaches to activity-based sensing: from metal sensors to bioorthogonal metal chemistry. *Inorg. Chem.* **58**, 13546–13560 (2019).
6. East, A. K., Lucero, M. Y. & Chan, J. New directions of activity-based sensing for *in vivo* NIR imaging. *Chem. Sci.* **12**, 3393–3405 (2021).
7. Pozzi, S. *et al.* Meet me halfway: Are *in vitro* 3D cancer models on the way to replace *in vivo* models for nanomedicine development? *Adv. Drug Deliv. Rev.* **175**, 113760 (2021).
8. Ast, T. & Mootha, V. K. Oxygen and mammalian cell culture: are we repeating the experiment of Dr. Ox? *Nat. Metab.* **1**, 858–860 (2019).
9. Yin, J. *et al.* Small molecule based fluorescent chemosensors for imaging the microenvironment within specific cellular regions. *Chem. Soc. Rev.* **50**, 12098–12150 (2021).
10. Li, H. *et al.* Activity-based smart AIEgens for detection, bioimaging, and therapeutics: Recent progress and outlook. *Aggregate* **2**, e51 (2021).
11. Bruemmer, K. J., Crossley, S. W. M. & Chang, C. J. Activity-based sensing: a synthetic methods approach for selective molecular imaging and beyond. *Angew. Chem. Int. Ed.* **59**, 13734–13762 (2020).
12. Sun, W., Li, M., Fan, J. & Peng, X. Activity-based sensing and theranostic probes based on photoinduced electron transfer. *Acc. Chem. Res.* **52**, 2818–2831 (2019).
13. Zhang, Y. *et al.* Rational construction of a reversible arylazo-based NIR probe for cycling hypoxia imaging *in vivo*. *Nat. Commun.* **12**, 2772 (2021).
14. Xu, H. *et al.* Tracking labile copper fluctuation *in vivo*/*ex vivo*: design and application of a ratiometric near-infrared fluorophore derived from 4-aminostyrene-conjugated boron dipyrromethene. *Inorg. Chem.* **60**, 18567–18574 (2021).
15. Zhang, T., Huo, F., Zhang, W., Chao, J. & Yin, C. Ultra-pH-sensitive sensor for visualization of lysosomal autophagy, drug-induced pH alteration and malignant tumors microenvironment. *Sensors Actuators, B Chem.* **345**, 130393 (2021).
16. Feng, W. *et al.* Lighting up NIR-II fluorescence *in vivo*: an activable probe for noninvasive hydroxyl radical imaging. *Anal. Chem.* **91**, 15757–15762 (2019).
17. Zhao, M., Li, B., Zhang, H. & Zhang, F. Activatable fluorescence sensors for *in vivo* bio-detection in the second near-infrared window. *Chem. Sci.* **12**, 3448–3459 (2021).
18. Inglut, C. T. *et al.* Predictors and limitations of the penetration depth of photodynamic effects in the rodent brain. *Photochem. Photobiol.* **96**, 301–309 (2020).
19. Richardson, D. S. *et al.* Tissue clearing. *Nat. Rev. Methods Prim.* **1**, 84 (2021).
20. Zhan, Y., Wu, H., Liu, L., Lin, J. & Zhang, S. Organic solvent-based tissue clearing techniques and their applications. *J. Biophotonics* e202000413 (2021).
21. Susaki, E. A. *et al.* Versatile whole-organ/body staining and imaging based on electrolyte-gel properties of biological tissues. *Nat. Commun.* **11**, 1982 (2020).
22. Pan, C. *et al.* Deep learning reveals cancer metastasis and therapeutic antibody targeting in the entire body. *Cell* **179**, 1661–1676 (2019).
23. Yang, B. *et al.* Single-cell phenotyping within transparent intact tissue through whole-body clearing. *Cell* **158**, 945–958 (2014).
24. Tainaka, K. *et al.* Whole-body imaging with single-cell resolution by tissue decolorization. *Cell* **159**, 911–924 (2014).
25. Eliat, F. *et al.* Tissue clearing may alter emission and absorption properties of common fluorophores. *Sci. Rep.* **12**, 5551 (2022).
26. Qi, Y. *et al.* FDISCO: Advanced solvent-based clearing method for imaging whole organs. *Sci. Adv.* **5**, eaau8355 (2019).
27. Lai, H. M. *et al.* Next generation histology methods for three-dimensional imaging of fresh and archival human brain tissues. *Nat. Commun.* **9**, 1066 (2018).
28. Nonaka, H. *et al.* Revisiting PFA-mediated tissue fixation chemistry: FixEL enables trapping of small molecules in the brain to visualize their distribution changes. *Chem* **9**, 1–18 (2023).
29. Mao, C. *et al.* Feature-rich covalent stains for super-resolution and cleared tissue fluorescence microscopy. *Sci. Adv.* **6**, eaba4542 (2020).
30. Fumoto, S. *et al.* A pH-adjustable tissue clearing solution that preserves lipid ultrastructures: Suitable tissue clearing method for DDS evaluation. *Pharmaceutics* **12**, 1070 (2020).
31. Evans, S. M. *et al.* Molecular probes for imaging of hypoxia in the retina. *Bioconjug. Chem.* **25**, 2030–2037 (2014).
32. Okuda, K. *et al.* 2-Nitroimidazole-tricarbocyanine conjugate as a near-infrared fluorescent probe for *in vivo* imaging of tumor hypoxia. *Bioconjug. Chem.* **23**, 324–329 (2012).
33. Zhu, H. *et al.* Imaging and profiling of proteins under oxidative conditions in cells and tissues by hydrogen-peroxide-responsive labeling. *J. Am. Chem. Soc.* **142**, 15711–15721 (2020).

34. Lee, S. *et al.* Activity-based sensing with a metal-directed acyl imidazole strategy reveals cell type-dependent pools of labile brain copper. *J. Am. Chem. Soc.* **142**, 14993–15003 (2020).
35. Dodt, H. U. *et al.* Ultramicroscopy: three-dimensional visualization of neuronal networks in the whole mouse brain. *Nat. Methods* **4**, 331–336 (2007).
36. Tainaka, K. *et al.* Chemical landscape for tissue clearing based on hydrophilic reagents. *Cell Rep.* **24**, 2196–2210 (2018).
37. Le Guern, F., Mussard, V., Gaucher, A., Rottman, M. & Prim, D. Fluorescein derivatives as fluorescent probes for pH monitoring along recent biological applications. *Int. J. Mol. Sci.* **21**, 9217 (2020).
38. Ma, Y., Chen, Q., Pan, X. & Zhang, J. Insight into fluorescence imaging and bioorthogonal reactions in biological analysis. *Top. Curr. Chem.* **379**, 10 (2021).
39. Matsumoto, K. *et al.* Advanced CUBIC tissue clearing for whole-organ cell profiling. *Nat. Protoc.* **14**, 3506–3537 (2019).
40. Mineno, T., Ueno, T., Urano, Y., Kojima, H. & Nagano, T. Creation of superior carboxyfluorescein dyes by blocking donor-excited photoinduced electron transfer. *Org. Lett.* **8**, 5963–5966 (2006).
41. Urano, Y. *et al.* Evolution of fluorescein as a platform for finely tunable fluorescence probes. *J. Am. Chem. Soc.* **127**, 4888–4894 (2005).
42. Whitaker, J. E. *et al.* Fluorescent rhodol derivatives: Versatile, photostable labels and tracers. *Anal. Biochem.* **207**, 267–279 (1992).
43. Chu, Y. *et al.* Development of theragnostic tool using NIR fluorescence probe targeting mitochondria in glioma cells. *Bioconjug. Chem.* **30**, 1642–1648 (2019).
44. Sung, J. *et al.* A new infrared probe targeting mitochondria via regulation of molecular hydrophobicity. *Bioconjug. Chem.* **30**, 210–217 (2019).
45. Koide, Y., Urano, Y., Hanaoka, K., Terai, T. & Nagano, T. Evolution of group 14 rhodamines as platforms for near-infrared fluorescence probes utilizing photoinduced electron transfer. *ACS Chem. Biol.* **6**, 600–608 (2011).
46. Grzybowski, M. *et al.* A highly photostable near-infrared labeling agent based on a phospha-rhodamine for long-term and deep imaging. *Angew. Chem. Int. Ed.* **57**, 10137–10141 (2018).
47. Karolin, J., Johansson, L. B. A., Strandberg, L. & Ny, T. Fluorescence and absorption spectroscopic properties of dipyrrometheneboron difluoride (BODIPY) derivatives in liquids, lipid membranes, and proteins. *J. Am. Chem. Soc.* **116**, 7801–7806 (1994).
48. Han, J. S. *et al.* Adipocyte HIF2α functions as a thermostat via PKA Cα regulation in beige adipocytes. *Nat. Commun.* **13**, 3268 (2022).
49. Catrina, S. B. & Zheng, X. Hypoxia and hypoxia-inducible factors in diabetes and its complications. *Diabetologia* **64**, 709–716 (2021).
50. Burtscher, J., Mallet, R. T., Burtscher, M. & Millet, G. P. Hypoxia and brain aging: Neurodegeneration or neuroprotection? *Ageing Res. Rev.* **68**, 101343 (2021).
51. Lee, P., Chandel, N. S. & Simon, M. C. Cellular adaptation to hypoxia through hypoxia inducible factors and beyond. *Nat. Rev. Mol. Cell Biol.* **21**, 268–283 (2020).
52. Cordeiro, I. R. *et al.* Environmental oxygen exposure allows for the evolution of interdigital cell death in limb patterning. *Dev. Cell* **50**, 155–166 (2019).
53. Arteel, G. E., Thurman, R. G. & Raleigh, J. A. Reductive metabolism of the hypoxia marker pimonidazole is regulated by oxygen tension independent of the pyridine nucleotide redox state. *Eur. J. Biochem.* **253**, 743–750 (1998).
54. Haase, V. H. Mechanisms of hypoxia responses in renal tissue. *J. Am. Soc. Nephrol.* **24**, 537–541 (2013).
55. Coblin, W. S., Lau, U. & Hongyin, N. Hypoxia of the renal medulla – Its implications for disease. *Monum. Serica* **41**, 299–347 (1993).
56. Inoue, M., Saito, R., Kakita, A. & Tainaka, K. Rapid chemical clearing of white matter in the post-mortem human brain by 1,2-hexanediol delipidation. *Bioorg. Med. Chem. Lett.* **29**, 1886–1890 (2019).
57. Hsu, C.-W. *et al.* EZ Clear for simple, rapid, and robust mouse whole organ clearing. *elife* **11**, e77419 (2022).
58. Honeycutt, S. E. & O'Brien, L. L. Injection of Evans blue dye to fluorescently label and image intact vasculature. *Biotechniques* **70**, 181–185 (2020).
59. Lübbers, D. W. & Baumgärtl, H. Heterogeneities and profiles of oxygen pressure in brain and kidney as examples of the pO_2 distribution in the living tissue. *Kidney Int.* **51**, 372–380 (1997).
60. Mizukami, K. *et al. In vivo* O_2 imaging in hepatic tissues by phosphorescence lifetime imaging microscopy using Ir(III) complexes as intracellular probes. *Sci. Rep.* **10**, 21053 (2020).
61. Brooks, A. J., Eastwood, J., Beckingham, I. J. & Girling, K. J. Liver tissue partial pressure of oxygen and carbon dioxide during partial hepatectomy. *Br. J. Anaesth.* **92**, 735–737 (2004).
62. Caldwell, C. C. *et al.* Differential effects of physiologically relevant hypoxic conditions on T lymphocyte development and effector functions. *J. Immunol.* **167**, 6140–6149 (2001).
63. Wadghiri, Y. Z. *et al.* High-resolution imaging of myeloperoxidase activity sensors in human cerebrovascular disease. *Sci. Rep.* **8**, 7687 (2018).